

Article

# Near Room Temperature Light-Activated WS<sub>2</sub>-Decorated rGO as NO<sub>2</sub> Gas Sensor

Valentina Paolucci <sup>1,\*</sup> , Seyed Mahmoud Emamjomeh <sup>1</sup>, Luca Ottaviano <sup>2,3</sup> and Carlo Cantalini <sup>1</sup>

<sup>1</sup> Department of Industrial and Information Engineering and Economics, Via G. Gronchi 18, University of L'Aquila, I-67100 L'Aquila, Italy; seyedmahmoud.emamjomeh@graduate.univaq.it (S.M.E.); carlo.cantalini@univaq.it (C.C.)

<sup>2</sup> Department of Physical and Chemical Sciences, Via Vetoio 10, University of L'Aquila, I-67100 L'Aquila, Italy; luca.ottaviano@aquila.infn.it

<sup>3</sup> CNR-SPIN Uos L'Aquila, Via Vetoio 10, I-67100 L'Aquila, Italy

\* Correspondence: valentina.paolucci2@graduate.univaq.it; Tel.: +39-328-952-5503

Received: 10 May 2019; Accepted: 6 June 2019; Published: 9 June 2019



**Abstract:** The NO<sub>2</sub> response in the range of 200 ppb to 1 ppm of a chemoresistive WS<sub>2</sub>-decorated rGO sensor has been investigated at operating temperatures of 25 °C and 50 °C in dry and humid air (40% RH) under dark and Purple Blue (PB) light conditions ( $\lambda = 430$  nm). Few-layers WS<sub>2</sub>, exfoliated by ball milling and sonication technique, with average dimensions of 200 nm, have been mixed with rGO flakes (average dimension 700 nm) to yield WS<sub>2</sub>-decorated rGO, deposited on Si<sub>3</sub>N<sub>4</sub> substrates, provided with platinum (30  $\mu$ m gap distance) finger-type electrodes. TEM analysis showed the formation of homogeneous and well-dispersed WS<sub>2</sub> flakes distributed over a thin, continuous and uniform underlying layer of interconnected rGO flakes. XPS and STEM revealed a partial oxidation of WS<sub>2</sub> flakes leading to the formation of 18% amorphous WO<sub>3</sub> over the WS<sub>2</sub> flakes. PB-light irradiation and mild heating of the sensor at 50 °C substantially enhanced the baseline recovery yielding improved adsorption/desorption rates, with detection limit of 400 ppb NO<sub>2</sub> and reproducible gas responses. Cross sensitivity tests with humid air interfering vapor highlighted a negligible influence of water vapor on the NO<sub>2</sub> response. A charge carrier mechanism between WS<sub>2</sub> and rGO is proposed and discussed to explain the overall NO<sub>2</sub> and H<sub>2</sub>O response of the WS<sub>2</sub>-rGO hybrids.

**Keywords:** WS<sub>2</sub>-rGO hybrids; chemoresistive sensors; NO<sub>2</sub>; Purple Blue light activation

## 1. Introduction

The intrinsic merits of Transition Metal Dichalcogenides (TMDs), including their high surface-to-volume ratio and semiconducting properties, have accelerated the development of a diverse range of applications of these materials as chemical sensors [1,2]. Two-dimensional (2D) mono- or few-layer TMDs produced by different exfoliation procedures, expose both plate and edge atoms of a single layer capable of adsorbing gas molecules, providing the largest sensing area per unit volume. Among a large variety of gaseous species, NO<sub>2</sub>, H<sub>2</sub> and NH<sub>3</sub> are the most investigated gases, considering their high chemical reactivity with mono- or few-layer MoS<sub>2</sub> [3–5], WS<sub>2</sub> [6,7], MoSe<sub>2</sub> [8] and MoTe<sub>2</sub> [9].

In need to decrease the operating temperature of the sensing materials, a common drawback of TMDs operating at room temperature, is their slow response and recovery times, or even no recovery when used at low temperatures [3,5,10]. The increase of the operating temperature up to 150 °C greatly improves adsorption/desorption rates and baseline recovery, but causes partial oxidation of TMDs into their metal oxide counterparts, as previously demonstrated for MoS<sub>2</sub> and WS<sub>2</sub>-layered materials [5,7,11]. It turns out that both low and high temperatures hinder the practical use of TMDs due to kinetic (i.e., slow recovery rates) and thermodynamical (i.e., spontaneous oxidation) reasons,

respectively. A possible strategy to avoid irreversible adsorption and ageing phenomena, and thus, to enhance the long term stability of the sensors, is to operate them at low temperature utilizing light irradiation as an external source of energy, as previously reported for metal oxide sensors [12,13], rGO-Metal Oxide nanocomposite [14], graphene [15], MoS<sub>2</sub> [3] and WS<sub>2</sub> [16].

Considering the variety of different preparation techniques for producing mono- or few-flake TMDs, consistent with standard electronic processes, some other aspects must be considered. A first issue is the reproducibility of the exfoliation procedure with respect to both microstructure (i.e., number of layers, lateral size, surface area, etc.) and chemical composition (i.e., defects concentration and surface oxidation). A second aspect is the small allowable average lateral size of the TMDs flakes, which may range from 100 to 300 nm, depending on the exfoliation technique [17]. A final issue is the surface coverage of the substrate, needed to create percolation paths for charge carriers between TMDs flakes, bridging metal electrodes. The possibility of using hybrid nanostructures, mostly focused on MoS<sub>2</sub>/graphene, making use of large-size, conducting-flakes-pathways of Graphene Oxide (GO) or reduced Graphene Oxide (rGO) with dispersed smaller-size, lesser-conductive-flakes of MoS<sub>2</sub> has been recently reported as an effective solution to enhance the fabrication of this new class of gas sensors [18–20]. Beside some reports on the utilization of WS<sub>2</sub>/GO hybrids as electrocatalysts for hydrogen evolution reactions [21,22] and WS<sub>2</sub>/GO as humidity [23] and NH<sub>3</sub> [24] sensors, no applications of WS<sub>2</sub>-rGO nanocomposite for NO<sub>2</sub> gas sensing applications have been reported so far.

In this paper, we report the exfoliation of WS<sub>2</sub> powders by a combined ball milling and sonication technique, which leads to average dimensions of 200 nm and “aspect ratios”, i.e., lateral dimension to the thickness of 27, to produce mono to few-layer WS<sub>2</sub> with controlled morphology and chemical composition. WS<sub>2</sub> flakes are mixed with rGO flakes with average dimensions of 700 nm to yield WS<sub>2</sub>-decorated rGO as chemoresistive NO<sub>2</sub> thin films deposited on large-area Si<sub>3</sub>N<sub>4</sub> substrates, provided with platinum finger-type patterned electrodes.

The aim of this paper is firstly to demonstrate the reliability of the decoration process leading to the deposition of thin films of well dispersed WS<sub>2</sub> flakes over large-size, interconnected rGO flakes, secondly, to demonstrate and discuss the influence of purple blue light ( $\lambda = 430$  nm) to detect NO<sub>2</sub> gas in air in the operating temperature range of 25 °C to 50 °C, and lastly, to investigate the influence of water vapor on the NO<sub>2</sub> gas response.

## 2. Materials and Methods

**Materials Preparation.** GO was prepared via a modified Hummers method [25] starting from graphite flakes of 500  $\mu$ m maximum size. Monolayers with average sizes of several micrometres and thicknesses of less than 2 nm were obtained and dispersed in water to reach a final concentration of 0.05 mg/mL. Two-dimensional WS<sub>2</sub> flakes, with average lateral size of 200 nm and average thickness under 15 nm, were obtained by starting from WS<sub>2</sub> commercial powder (Sigma-Aldrich 243639-50G) exfoliated by ball milling assisted sonication, and dispersed in ethanol and subsequently centrifuged as described in the Supporting Figure S1. Finally, equal amounts of the two GO/water and WS<sub>2</sub>/ethanol solutions were mixed together and sonicated for 10 min to homogenize the dispersion and avoid agglomeration.

**Microstructural and chemical characterization.** TEM and STEM pictures of the WS<sub>2</sub>-decorated GO were acquired using a TEM—JEOL 2100 Field Emission Transmission Electron Microscope operating at 200 kV by drop casting the dispersion on a lacey grid. Samples prepared by drop casting the WS<sub>2</sub>-GO dispersion on Si<sub>3</sub>N<sub>4</sub> substrates were further analyzed by X-Ray Photoemission Spectroscopy (XPS) using a PHI 1257 spectrometer equipped with a monochromatic Al K $\alpha$  source ( $h\nu = 1486.6$  eV) with a pass energy of 11.75 eV (93.9 eV survey), corresponding to an overall experimental resolution of 0.25 eV. Thin-film XRD measurements were performed at 3° incidence using a Philips PW1710 diffractometer equipped with grazing-incidence X-ray optics, using Cu K $\alpha$  Ni-filtered radiation at 30 kV and 40 mA.

**Sensor fabrication and gas sensing measurements:** Thin layers have been prepared by drop casting 8  $\mu$ L of the water/ethanol dispersed WS<sub>2</sub>-GO solution on Si<sub>3</sub>N<sub>4</sub> substrates provided with 30  $\mu$ m

spaced Pt interdigitated electrodes, followed by annealing at 70 °C for 30 min to partially reduce the GO to rGO in order to fix the film resistivity in the range of  $10^4$ – $10^5$  Ohm. The electrical resistance of the sensors was measured by an automated system. The sensors placed inside a Teflon chamber ( $500\text{ cm}^3$ ), provided with Teflon tubings have been exposed to different gas concentrations in the range 200 ppb–10 ppm  $\text{NO}_2$  obtained by mixing certified  $\text{NO}_2$  mixtures with dry air carrier gas at 500 sccm/min flow rate, by means of an MKS147 multi gas mass controller. Electrical resistance was measured by a volt-amperometric technique (AGILENT 34970A) under dark and Purple Blue (PB) light irradiating conditions (PB  $\lambda = 430\text{ nm}$ ) and different power densities at  $270\text{ }\mu\text{W}/\text{cm}^2$ ,  $468\text{ }\mu\text{W}/\text{cm}^2$  and  $668\text{ }\mu\text{W}/\text{cm}^2$ . The device temperature has been controlled by heating elements and temperature sensors (thermocouples) integrated on the device backside, guaranteeing that the gas pressure was not affected by the changes in the OT.

In this paper the relative response  $RR$  is represented by the ratio  $RR = R_a/R_g$  where  $R_a$  and  $R_g$  are the resistances in dry air and in gas respectively and  $\tau_{\text{ads}}$  and  $\tau_{\text{des}}$  (respectively adsorption and desorption times) represent the time required to reach 90% of the full response at equilibrium, during both gas adsorption and desorption.

### 3. Results and Discussion

#### 3.1. Morphological and Compositional Characterization of the $\text{WS}_2$ -Decorated rGO

Thin films of  $\text{WS}_2$ -decorated rGO deposited on  $\text{Si}_3\text{N}_4$  substrates provided with Pt finger type electrodes have been characterized. We have firstly deposited by drop deposition the minimum amount of  $\text{WS}_2$ -rGO solution, corresponding to the formation of a continuous percolation path of GO flakes. The development of a continuous percolation path was assessed by recording the electrical resistance of the film corresponding to the onset of an electrical contact between the electrodes ( $30\text{ }\mu\text{m}$  apart). By further annealing at 70 °C in air for 30 min, the GO flakes have been partially reduced to rGO to yield baseline resistances in air in the range of  $10^4$ – $10^5\text{ }\Omega$ .

The  $\text{WS}_2$ -decorated rGO morphology was first characterized by low-resolution TEM, as shown in Figure 1a.  $\text{WS}_2$  flakes (darker regions) are distributed over a thin, continuous and uniform layer made of interconnected rGO flakes (light-grey background) as revealed by the presence of grey lines attesting the formation of rGO folded edges (yellow arrows in Figure 1a). Statistical image analysis carried out on differently prepared samples over an area of  $80\text{ }\mu\text{m}^2$ , as shown in Figure 1b, exhibits a log-normal  $\text{WS}_2$  average particle size distribution with an average particle size dimension of 200 nm and an average  $\text{WS}_2$  flakes coverage percentage of 6%. Notably, the dispersion of the  $\text{WS}_2$  flakes is homogeneous over the investigated area, meaning that the sonication step after mixing represents an effective strategy to avoid agglomeration of the  $\text{WS}_2$  flakes.

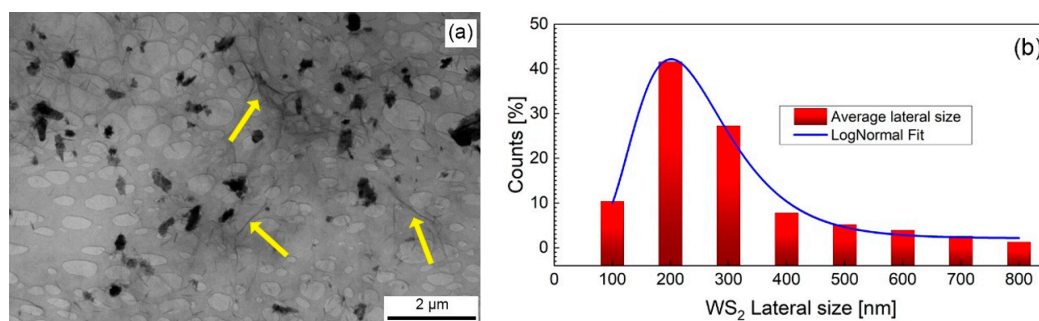


**Figure 1.** (a) Low-resolution TEM image of  $\text{WS}_2$ -decorated GO deposited on a lacey grid.  $\text{WS}_2$  flakes (darker regions) distributed over interconnected rGO flakes (light-grey background). The occurrence of grey lines (highlighted by yellow arrows) attest the formation of rGO folded edges; (b) Lateral size distribution of  $\text{WS}_2$  flakes and corresponding Log Normal fit.

The TEM analysis shown in Figure 2a reveals the presence of large (i.e., hundreds of nanometers) transparent, irregularly shaped GO flakes with folded edges (yellow arrow) distributing according to a continuous planar underlying layer. From Figure 2a it is shown that WS<sub>2</sub> flakes may also align vertically, as highlighted by the darker needle-shaped formations inside the red circles of Figure 2a. Statistical analysis carried out on the vertically aligned WS<sub>2</sub> flakes revealed an average thickness of 15 nm, corresponding approximately to 25 layers. TEM image depicted in Figure 1b illustrates the formation of well-shaped, stacked-few-layers WS<sub>2</sub>, with edge angles of 120°, deposited over the underlying GO flakes. The crystalline nature of few-flakes WS<sub>2</sub> is confirmed by the selected area electron diffraction (SAED) pattern shown in the inset of Figure 2b, which clearly exhibits the formation of WS<sub>2</sub> nanosheet with hexagonal atomic arrangements, assigned to WS<sub>2</sub> (100) plane [26].

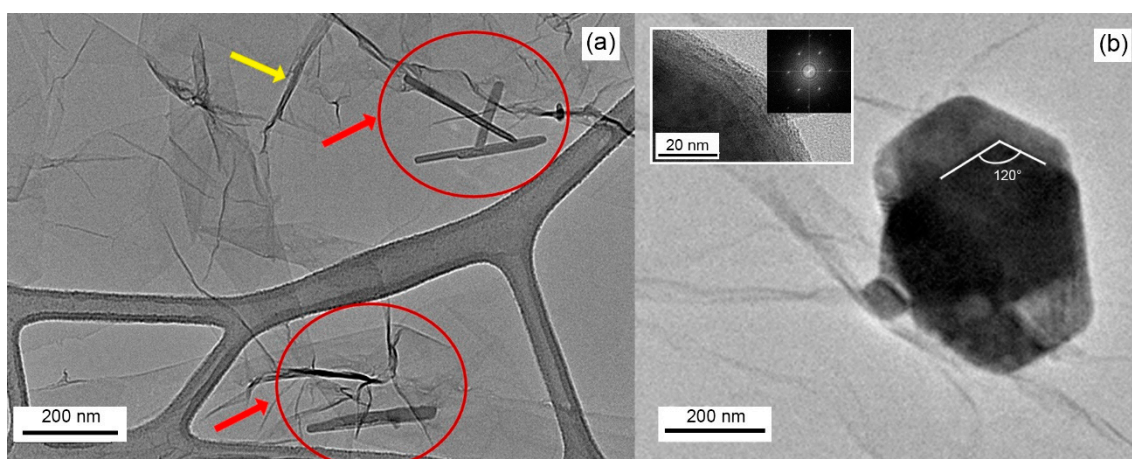
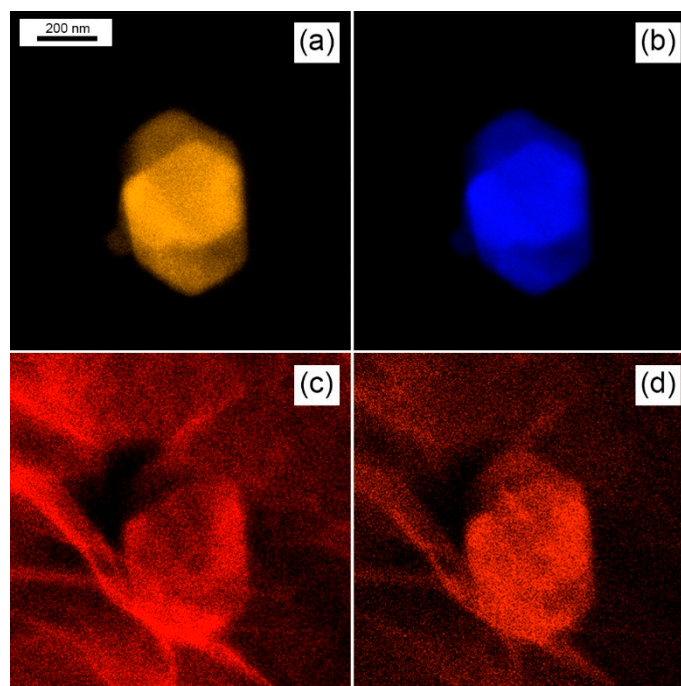


**Figure 2.** High-resolution TEM of WS<sub>2</sub>-decorated rGO showing: (a) light-grey background of interconnected GO flakes. Darker grey lines (yellow arrow) corresponding to folded GO edges and some WS<sub>2</sub> flakes vertically placed on GO flakes (needless inside the red circle); (b) a big hexagonal WS<sub>2</sub> flake. The inset shows a magnification of the flake's edges with related SAED analysis pattern.

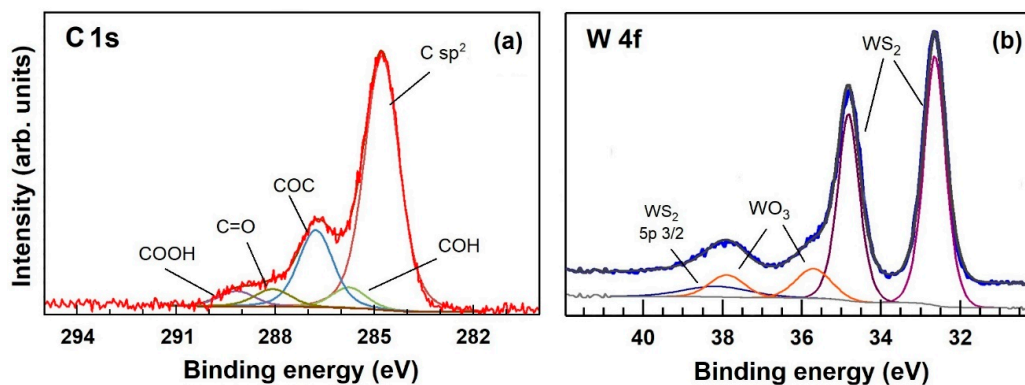
Figure 3 shows the atomic distribution of sulphur (a), tungsten (b), carbon (c) and oxygen (d) elements, as measured by STEM technique, respectively on the sample displayed in Figure 2b. From Figure 3a,b, it turns out that the distribution of tungsten and sulphur exactly replicates the shape of the WS<sub>2</sub> flake. The carbon signal over the WS<sub>2</sub> particles of Figure 3c, may be possibly be attributed to a partial contamination of the sample, whereas the carbon signal deriving from the background, clearly replicates the morphology of the rGO underlying layer. The chromatic signal intensity of oxygen corresponding to the WS<sub>2</sub> flake (Figure 3d), is slightly brighter than the background, indicating the occurrence of a higher oxygen concentration over the WS<sub>2</sub> flake with respect to the rGO background, suggesting the occurrence of an oxidation process of WS<sub>2</sub>, as it will be confirmed in the next XPS section.

Figure 4 shows the XPS C1s (a) and W4f (b) core level photoemission spectra of WS<sub>2</sub>-decorated rGO air-annealed at 70 °C. According to the literature [27,28], the C1s spectrum shown in Figure 4a has been successfully fitted by the sum of five components assigned to C sp<sup>2</sup> atoms belonging to aromatic rings and hydrogenated carbon (C=C/C–C 284.7 eV), hydroxyl groups (C–OH, 285.8 eV), epoxy groups (C–O–C, 286.8 eV), carbonyl groups (C=O, 288.0 eV), and carboxyl groups (C=O(OH), 289.2 eV). Upon thermal annealing at 70 °C, the intensity of all the oxygen-containing groups is lowered, with regard to sp<sup>2</sup> carbon containing ones (i.e., (C=C/C–C), signifying a loss of oxygen in favor of sp<sup>2</sup> carbon. Compared to previous results [29], the XPS spectrum shown in Figure 4a is located halfway between the XPS signals of as deposited GO and the one corresponding to 200 °C UHV-annealed rGO. Regarding the tungsten W4f of Figure 4b, the four peaks fitting the spectrum can be located, according to the literature [30,31], to WS<sub>2</sub> and WO<sub>3</sub>. These results suggest, as previously reported for MoS<sub>2</sub> and WS<sub>2</sub> [5,7,11], that crystalline WS<sub>2</sub> is partially oxidized to WO<sub>3</sub> with an associated content of

approximately 18%. Grating incidence XRD measurements on the  $WS_2$ -decorated rGO annealed at 70 °C for 30 min, as shown in the supporting Figure S2, revealed that the  $WO_3$  is amorphous.



**Figure 3.** STEM elemental mapping of the flake shown in Figure 2b showing the atomic distribution of: (a) sulfur, (b) tungsten, (c) carbon and (d) oxygen.



**Figure 4.** XPS spectra of the  $WS_2$ -decorated rGO showing (a) C1s core level spectrum of rGO flakes and (b) W 4f core level spectrum of  $WS_2$ .

### 3.2. $NO_2$ Gas Response

The reacting surface of the  $WS_2$ -decorated rGO comprises, as attested by microstructural characterization, a flat underlying layer made of large and interconnected rGO flakes covered with dispersed, partially oxidized,  $WS_2$  flakes. Given that  $WS_2$  flakes do not form a continuous layer (see Figure 1a), it is the rGO layer which mostly determines the baseline resistance of the  $WS_2$ -rGO hybrid. The  $NO_2$  gas responses in dry air of a single rGO film and a  $WS_2$ -decorated rGO film at 25 °C and 50 °C operating temperatures (OT) are compared in Figure 5.

By increasing the OT to 50 °C, the baseline resistance (BLR) of the  $WS_2$ -decorated rGO (dotted lines in the figure) decreases almost of one decade as compared to rGO, attesting the substantial contribution of the  $WS_2$  semiconductor to the overall resistance response. At 25 °C OT, by increasing the  $NO_2$  gas concentration, it is noted that: (i) the baseline resistance (BLR) is not recovered after gas

desorption; (ii) baseline resistance steadily drifts, decreasing its resistance; (iii) the electrical signal never reaches equilibrium under adsorption/desorption conditions within the time schedule of the experiment (i.e., 60 min). Conversely, by increasing the OT to 50 °C, WS<sub>2</sub>-decorated rGO shows a faster response, improved equilibrium conditions and reduced baseline drift. Besides the positive effects related to the OT, it may be concluded that irreversible adsorption and baseline drift phenomena are still evident at 50 °C OT, representing a serious drawback for the exploitation of near room temperature WS<sub>2</sub>-rGO hybrids sensors.

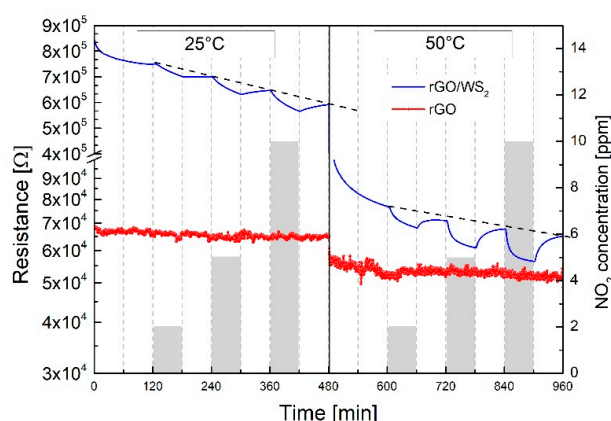


**Figure 5.** Electrical responses of single rGO (red line) and WS<sub>2</sub>-decorated rGO films (blue line) in dry air and NO<sub>2</sub> concentrations in the range 2–10 ppm at 25 °C and 50 °C operating temperature.

According to previous research which demonstrated the positive effect of the combined action of light irradiation and thermal activation on the NO<sub>2</sub> response of WO<sub>3</sub> and NiO semiconductor sensors [12,13], Figure 6 shows the rGO's and WS<sub>2</sub>-rGO hybrid's NO<sub>2</sub> gas responses at 25 °C in dry air under Purple Blue light (PB  $\lambda = 430$  nm @ 2.88 eV) and different power densities at 270  $\mu\text{W}/\text{cm}^2$ , 468  $\mu\text{W}/\text{cm}^2$  and 668  $\mu\text{W}/\text{cm}^2$ . Bare rGO exhibits neither significant changes of the electrical response at different power densities (in Figure 6 the response at 668  $\mu\text{W}/\text{cm}^2$  is shown) nor any appreciable gas response to 1 ppm NO<sub>2</sub>. WS<sub>2</sub>-decorated rGO yields relative responses ( $RR = R_a/R_g$  at 1ppm NO<sub>2</sub>) of approximately 1.21, more or less independent of the power density. Response and recovery times, in contrast, improve with increasing the power density.

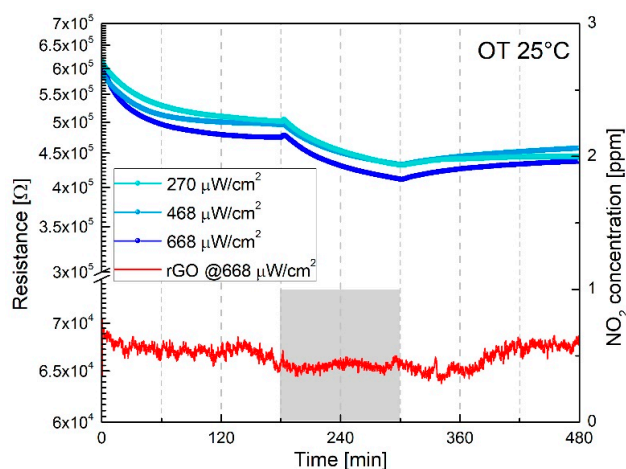


**Figure 6.** Response to 1 ppm NO<sub>2</sub> in dry air of WS<sub>2</sub>-decorated rGO and bare rGO film (red curve) irradiated by Purple-Blue ( $\lambda = 430$  nm) light at different power densities (270  $\mu\text{W}/\text{cm}^2$ , 468  $\mu\text{W}/\text{cm}^2$ , 668  $\mu\text{W}/\text{cm}^2$ ).

By selecting the  $668 \mu\text{W}/\text{cm}^2$  light power density, Figure 7 shows the electrical response of the  $\text{WS}_2$ -decorated rGO to 1 ppm  $\text{NO}_2$  in dry air under “dark” and “purple-blue” conditions at  $25^\circ\text{C}$  and  $50^\circ\text{C}$  OT respectively.

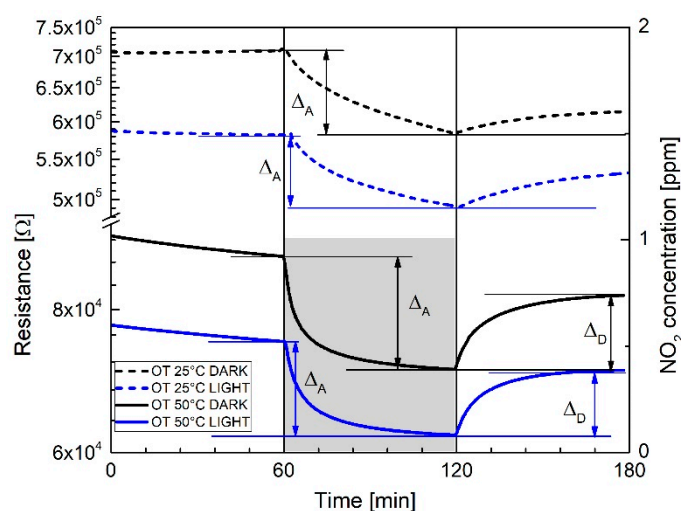


**Figure 7.** The 1 ppm  $\text{NO}_2$  gas responses of the  $\text{WS}_2$ -decorated rGO under “dark” and “light” conditions (dotted lines) at  $25^\circ\text{C}$  operating temperatures compared to the “dark” and light” conditions (solid lines) at  $50^\circ\text{C}$  operating temperature.

If we now define the recovery percentage ( $RP$ ) as the percentage ratio  $(\Delta_D/\Delta_A) \times 100$ , where  $\Delta_D$  and  $\Delta_A$  (see Figure 7) are the desorption/adsorption resistances’ variations ( $\Delta$ ), measured at the end of each desorption/adsorption cycle (i.e., 60 min), it turns out that light illumination strongly enhances the recovery of the baseline resistance during desorption.

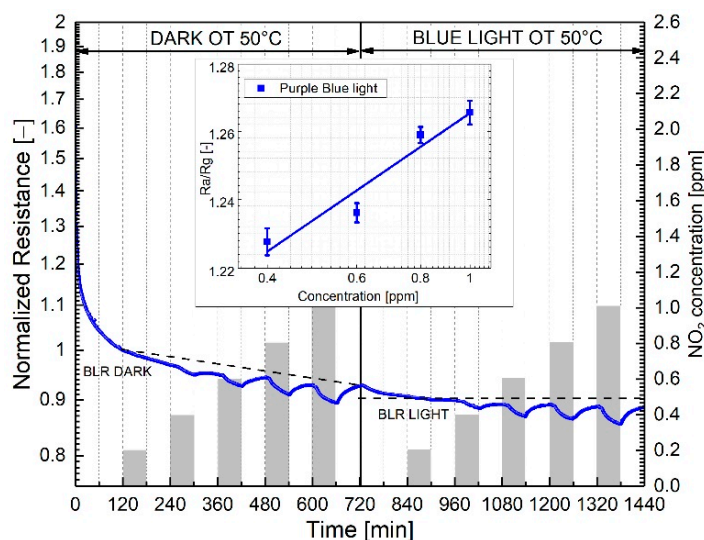
As shown in Figure 7 and Table 1, recovery percentage ( $RP$ ) values increase from 23% (dark) to 65% (light) at  $25^\circ\text{C}$  OT, and from 60% (dark) to 70% (light) at  $50^\circ\text{C}$  OT. Moreover, considering features and shapes of the curves displayed in Figure 7, at  $25^\circ\text{C}$  OT regardless of “dark” or “light” exposures, no equilibrium conditions are achieved within the timescale of the experiment (i.e., 60 min). In contrast, as attested by the horizontal slopes of the two bottom curves of Figure 7, equilibrium conditions are achieved under adsorption/desorption conditions when light irradiation is performed and when the OT is increased to  $50^\circ\text{C}$ . Notably, according to Table 1, given the associated uncertainty of the measurement ( $\pm 0.02$ ), no substantial changes of the relative responses’ values are recorded with respect to  $25^\circ\text{C}$ , either by increasing the OT to  $50^\circ\text{C}$  or by illuminating the sensor with purple blue light.

**Table 1.** Comparison of  $RR$ ,  $RP$ ,  $\tau_{\text{ads}}$  and  $\tau_{\text{des}}$  to 1 ppm  $\text{NO}_2$  in dark conditions and PB light illumination ( $\lambda = 430 \text{ nm}$  at  $668 \mu\text{W}/\text{cm}^2$ ) at different OT ( $25$ – $50^\circ\text{C}$ ). Notably (–) means that no equilibrium conditions have been reached within the time scale of the experiment.

Operating Conditions	Response TO 1 ppm $\text{NO}_2$			
	$RR$	$RP$	$\tau_{\text{ads}}$	$\tau_{\text{des}}$
	$R_a/R_g$	$\Delta_D/\Delta_A$		
	(–)	(%)	(min)	(min)
$25^\circ\text{C}$ DARK	$1.18 \pm 0.02$	23	–	–
$25^\circ\text{C}$ LIGHT	$1.21 \pm 0.02$	65	–	–
$50^\circ\text{C}$ DARK	$1.20 \pm 0.02$	60	22	26
$50^\circ\text{C}$ LIGHT	$1.27 \pm 0.02$	70	16	18

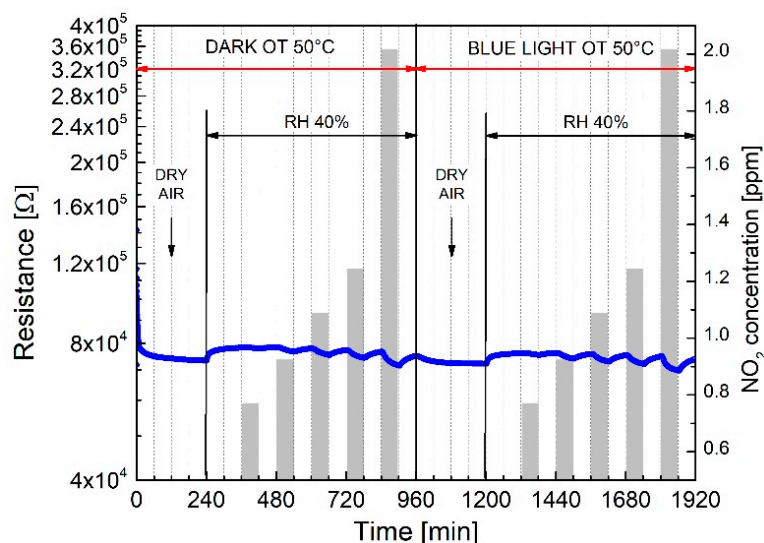
The results shown in Table 1 are in line, both in terms of sensitivity, using comparable definitions, and time constants with those reported in literature for hybrid graphene/MoS<sub>2</sub> structures for NO<sub>2</sub> sensing [18,19] working in dark conditions and at higher operating temperatures (at least 150 °C).

Figure 8 compares the normalized dynamic gas responses of the WS<sub>2</sub>-rGO sensor at 50 °C OT under dark and light conditions, respectively. By increasing the NO<sub>2</sub> concentration from 200 ppb to 1 ppm, purple blue light irradiation promotes full baseline recovery after each NO<sub>2</sub> pulse, as demonstrated by the horizontal slope of the dotted line of Figure 8. WS<sub>2</sub>-decorated rGO exhibits an experimental detection limit of 400 ppb NO<sub>2</sub> in dry air. The inset of Figure 8 shows the sensitivity plot of the response under PB illumination, with associated standard deviations. Reproducibility tests of the electrical response under pulse and cumulative NO<sub>2</sub> adsorption/desorption exposures, shown in the supporting Figure S3, exhibit no substantial irreversible adsorption phenomena, as well as a fairly good reproducibility of the electrical response. Additionally, long-term stability properties of the baseline and saturation resistances to 1 ppm NO<sub>2</sub> over a period of 12 months were also recorded. Supporting Figure S4 shows baseline resistances (upper curve) and saturation resistances corresponding to 1 ppm (lower curve), randomly collected over a period of 52 weeks, with associated standard deviations calculated over a set of five consecutive measurements. No remarkable fluctuations of both baseline and resistances at saturation are detectable, demonstrating good long-term stability properties of the WS<sub>2</sub> films.



**Figure 8.** Comparison of WS<sub>2</sub>-decorated rGO's electrical responses to increasing NO<sub>2</sub> concentrations at 50 °C operating temperature under dark and light conditions respectively. The inset shows the sensitivity plot corresponding to light conditions. The bars in the inset represent the standard deviation calculated over a set of five measurements performed for each gas concentration. Dotted lines indicate the baseline resistance in dry air.

The effect of 40% relative humidity (RH) to the NO<sub>2</sub> response, under dark and light conditions, at 50 °C OT, is shown in Figure 9. Regardless of the illumination: (i) the baseline resistance slightly increases from dry to humid (40% RH) conditions; (ii) the NO<sub>2</sub> relative responses ( $R_a/R_g$ ) at 40% RH, do not change appreciably neither under dark or light conditions; (iii) the baseline resistance is fully recovered after each adsorption/desorption cycle. This behavior demonstrates that humidity, regardless of the illumination conditions, does not appreciably interfere with the NO<sub>2</sub> gas adsorption mechanism, suggesting, as it will be discussed in the next paragraph, that NO<sub>2</sub> preferentially adsorbs on WS<sub>2</sub>, since energetically favored as respect to water vapor.



**Figure 9.** The influence of 40% Relative Humidity (40% RH) on the NO<sub>2</sub> response of WS<sub>2</sub>-decorated rGO under dark and light illumination at 50 °C operating temperature.

Finally, the sensors' selectivity among other interfering gases such as H<sub>2</sub>, NH<sub>3</sub>, acetone and ethanol has been recorded and the results shown in Supporting Figure S5. The WS<sub>2</sub>-decorated rGO sensor exhibits an excellent selectivity for NO<sub>2</sub> gas as compared to the other investigated species, making it suitable for being a selective NO<sub>2</sub> sensor.

#### Gas Sensing Mechanism

Discussing the gas sensing mechanism of the WS<sub>2</sub>-rGO hybrid sensor with respect to water vapor and NO<sub>2</sub>, the single contribution of the rGO and WS<sub>2</sub> species and WS<sub>2</sub>-rGO hybrid to the overall gas response have to be considered.

Regarding the single rGO in our previous work [29] we demonstrated that both as-deposited GO and partially reduced rGO (annealed in vacuum at 200 °C) exhibit a *p*-type response to NO<sub>2</sub>, resulting in a decrease of the resistance in the operating temperature range of 25–150 °C. Considering that the rGO prepared in this work shows a degree of reduction, located halfway between these two extremes, we would have expected a decrease of the resistance in Figure 5, rather than no response when exposing bare rGO film to NO<sub>2</sub> gas. The lack of any gas response may not be entirely attributed to the decrease of functional groups induced by the mild reduction process (i.e., air annealed at 70 °C), but mostly to a substantially smaller amount of the deposited rGO, which amounts to approximately 1/10 of the quantity previously utilized [29]. It may be concluded that the deposition procedure adopted here yields an rGO film which does not significantly contribute to the NO<sub>2</sub> response, while it guarantees the formation of a continuous, conductive layer “bridging” distant platinum finger-type electrodes.

Regarding single WS<sub>2</sub>, which is reported to increase its resistance to NO<sub>2</sub>, exhibiting an *n*-type response [7,16], some considerations apply. According to the XPS section, WS<sub>2</sub> flakes deposited on rGO partially oxidize to amorphous WO<sub>3</sub> (approx 18%). Amorphous WO<sub>3</sub>, as previously discussed [7,16], acts as a non-conductive phase, eventually inhibiting the charge-carrier transfer mechanism within the flakes. It turns out that the formation of WO<sub>3</sub>, while not contributing to the overall gas response, has the merely negative effect of partially covering the underlying reacting surface of the WS<sub>2</sub> flakes, eventually decreasing the relative gas response.

Regarding crystalline WS<sub>2</sub>, the variation of the electrical resistance induced by Air-NO<sub>2</sub> mixtures, is part of a complex mechanism involving the combined effects physisorption, chemisorption, the role of edges and surface defects and the transduction mechanism. First principle calculations on MoS<sub>2</sub> sulphur-vacancy-defective monolayers [32,33] demonstrated that O<sub>2</sub> firstly chemisorbs on existing sulphur vacancies, secondly, that sulphur vacancies are passivated (i.e., “healed”) by the dissociative

chemisorption of O<sub>2</sub> molecules, leading to the formation of two Mo-O bonds. In case of direct NO<sub>2</sub> molecules interaction with sulphur vacancies, a dissociative chemisorption of NO<sub>2</sub> takes place, leading to oxygen atoms passivating the vacancies (i.e., “secondary healing”) and NO molecules eventually to be physisorbed on the MoS<sub>2</sub> surface. Considering that both MoS<sub>2</sub> and WS<sub>2</sub>, are susceptible to spontaneous oxidation in air [11], the mechanism of sulphur vacancies suppression operated by O<sub>2</sub> and NO<sub>2</sub> claimed for MoS<sub>2</sub>, can be reasonably extended to sulphur defective WS<sub>2</sub>. Under these circumstances, literature reports based on first principle calculations on “healed” WS<sub>2</sub> surfaces pointed out that O<sub>2</sub>, NO<sub>2</sub> and H<sub>2</sub>O physisorb on defect-free monolayer WS<sub>2</sub> surfaces [34,35].

Regarding WS<sub>2</sub>-rGO hybrids, they decrease their overall resistance when exposed to NO<sub>2</sub> (see Figure 5), exhibiting, as reported for MoS<sub>2</sub>/Graphene composites [18,20], an overall *p*-type response. Bearing in mind that the WS<sub>2</sub>-rGO hybrid’s gas response depends on both charge transfer values (positive charge transfer values between adsorbing molecules and the material surface stand for electrons withdrawal from the material) and adsorption energies (negative adsorption energy means that the adsorption process is exothermic and energetically favourable), the following discussion applies.

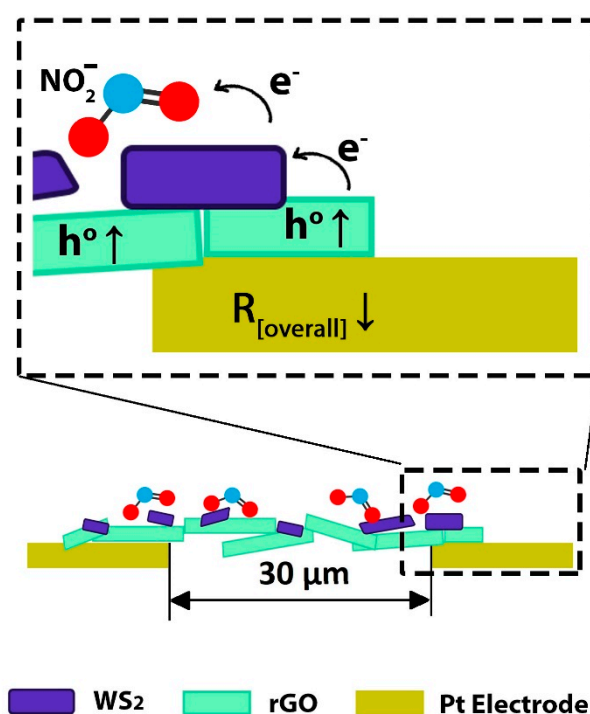
According to Table 2, adsorption of a single NO<sub>2</sub> molecule on rGO yields charge transfer values of approximately 0.029e and associated adsorption energies of −0.80 eV [32,34,35]. By contrast, the adsorption of a single NO<sub>2</sub> molecule on defect free WS<sub>2</sub> indicate that NO<sub>2</sub> physisorbs on WS<sub>2</sub> yielding charge transfer values of 0.178e and associated adsorption energies of −0.41 eV [34,35].

**Table 2.** Adsorption energy on rGO and WS<sub>2</sub> of O<sub>2</sub>, NO<sub>2</sub> and H<sub>2</sub>O molecules. Note that negative adsorption energy means that the adsorption process is exothermic and energetically favorable.

Physisorbed Molecules	Adsorption Energy on rGO (eV)	Reference	Adsorption Energy on WS <sub>2</sub> (eV)	Reference
O <sub>2</sub>	−0.16	[36]	−0.24	[36]
NO <sub>2</sub>	−0.80	[32,34,35]	−0.41	[34,35]
H <sub>2</sub> O	−0.04	[37]	−0.23	[34]

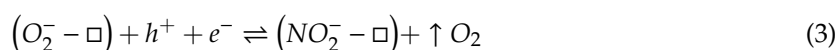
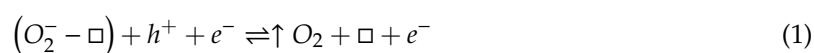
Considering that calculated NO<sub>2</sub> charge transfer values are 0.029e for rGO and 0.178e for WS<sub>2</sub>, it turns out that WS<sub>2</sub> yields a net charge transfer 6.14 times higher than on of rGO per NO<sub>2</sub> physisorbed molecule. Given these premises, the electrical response of WS<sub>2</sub>-decorated rGO as compared to single rGO shown in Figure 5, accounts for the larger WS<sub>2</sub>’s charge carrier exchange with respect to rGO.

Figure 10, which is a schematic illustration of the WS<sub>2</sub>-decorated rGO film, deposited between two platinum electrodes 30 μm apart, highlights that NO<sub>2</sub> molecules adsorbs on both rGO and WS<sub>2</sub> causing electrons to withdraw from both materials. Considering the smaller charge transfer induced by NO<sub>2</sub> adsorption on rGO (i.e., 0.029e) with respect to WS<sub>2</sub> (i.e., 0.178e), by exposing the WS<sub>2</sub>-rGO hybrid to NO<sub>2</sub> gas, the NO<sub>2</sub> gas molecule withdraws electrons mainly from the WS<sub>2</sub> surface. As a consequence, electron-depleted *n*-type WS<sub>2</sub> flakes drain electrons from the underlying *p*-type rGO, thanks to a rapid electron transport from the highly conducting rGO to the less-conducting WS<sub>2</sub> [19,22]. The increase of hole concentration in *p*-type rGO due to physisorption of NO<sub>2</sub> molecules on WS<sub>2</sub> flakes, explains the decrease of the overall resistance of the *p*-type WS<sub>2</sub>-decorated rGO shown in Figure 5. It may be concluded that rGO flakes, with excellent transport capability, serve as highly conductive channels bridging distant electrodes, whereas WS<sub>2</sub> decoration eventually modulates the NO<sub>2</sub> gas response.



**Figure 10.** Schematic illustration of the proposed sensing mechanism of WS<sub>2</sub>-decorated rGO hybrid during NO<sub>2</sub> exposure.

Regarding the influence of purple–blue light, it is well known that response and recovery rates depend on the adsorption energy of the adsorbed gas molecules (see Table 2). Light irradiation and thermal activation represent, therefore, two alternative or complementary modes to improve response/recovery rates [13]. By irradiating WS<sub>2</sub>-decorated rGO with purple–blue light (PB  $\lambda = 430$  nm) the associated photon energy of 2.88 eV and power density of 668  $\mu\text{W}/\text{cm}^2$  provide: (i) a large quantity of photo generated electrons/holes; (ii) the required energy to desorb physisorbed O<sub>2</sub>, NO<sub>2</sub> and H<sub>2</sub>O molecules from both rGO and WS<sub>2</sub> flakes. Under NO<sub>2</sub> gas and PB light illumination, physisorbed oxygen partially desorbs from its adsorption site ( $\square$ ) according to Reaction (1) while NO<sub>2</sub> physisorbs on free sites ( $\square$ ) left behind from oxygen desorption according to Reaction (2). At equilibrium the overall reaction is represented by Equation (3).



Considering that NO<sub>2</sub> molecules withdraw electrons with an associated charge transfer of 0.178e as compared to that of Oxygen of 0.136e [34], under NO<sub>2</sub> adsorption, Equation (3) is shifted to the right, meaning an excess of holes, which explains the overall resistance decrease of the WS<sub>2</sub>-rGO hybrid. Moreover, the improved recovery percentages and response times of Figure 7, account for the extra light-photogenerated carriers which speed up the time to reach equilibrium (Equation (3)) both during gas exposure and recovery.

Regarding water interaction with WS<sub>2</sub>-rGO hybrid the reason why humidity, regardless of the illumination conditions, does not appreciably interfere with the NO<sub>2</sub> gas response, can be tentatively explained (see Table 2) evaluating that the adsorption energy of a NO<sub>2</sub> molecule on WS<sub>2</sub> is approximately twice (−0.41 eV) the corresponding energy of water (−0.23 eV), indicating a stronger attitude of NO<sub>2</sub> molecules to adsorb on WS<sub>2</sub> compared to water. Finally, the initial resistance increase of the WS<sub>2</sub>-rGO

when exposed to humid air can be explained taking into consideration that water is a reducing agent, which adsorbs on both rGO and WS<sub>2</sub> injecting electrons, thus decreasing the hole concentration in rGO and WS<sub>2</sub>, causing an overall resistance increase of the WS<sub>2</sub>-rGO hybrid.

#### 4. Conclusions

We have exfoliated, by a combined grinding and sonication technique, WS<sub>2</sub> commercial powders into mono-to few-layer flakes of WS<sub>2</sub>, with an average dimension of 200 nm, which have been successfully dispersed with rGO flakes with average dimensions of 700 nm, to yield WS<sub>2</sub>-decorated rGO as chemo-resistive NO<sub>2</sub> thin film sensor. Operating at near room temperature conditions and providing an extra source of energy, by purple-blue light illumination, we have proposed a possible strategy to improve adsorption/desorption rates and to suppress water vapour cross sensitivity. The deposition procedure adopted here yields WS<sub>2</sub> flakes which mostly drive the NO<sub>2</sub> gas response, while the underlying rGO film guarantees the formation of a continuous, conductive layer “bridging” distant platinum finger-type electrodes. By retrieving literature data about charge carriers and adsorption energies deriving from the interaction of NO<sub>2</sub>, O<sub>2</sub> and water molecules with WS<sub>2</sub> and rGO, we have proposed a gas sensing mechanism which accounts for the overall gas response of the WS<sub>2</sub>-rGO hybrids.

**Supplementary Materials:** The following are available online at <http://www.mdpi.com/1424-8220/19/11/2617/s1>, Figure S1: Schematic illustration of WS<sub>2</sub> exfoliation process, Figure S2: Grazing incidence XRD spectrum of WS<sub>2</sub>-decorated rGO film, Figure S3: Reproducibility and base line recovery features of the WS<sub>2</sub>-decorated rGO by exposing the film to both dynamic and cumulative NO<sub>2</sub> concentrations (5–10 ppm) under light irradiation (purple blue), Figure S4. Long term stability properties of the WS<sub>2</sub>/rGO hybrid sensor, Selectivity response of the the WS<sub>2</sub>/rGO hybrid sensor to different oxidizing and reducing gases, measured at 50 °C operating temperature under purple-blue illumination.

**Author Contributions:** Conceptualization, L.O., C.C and V.P.; investigation, V.P. and S.M.E.; data curation, V.P.; Methodology, L.O. and C.C.; Formal analysis, V.P.; writing—original draft preparation, C.C. and V.P.; writing—review and editing, L.O., C.C.

**Funding:** This research was funded by REGIONE ABRUZZO Dipartimento Sviluppo Economico, Politiche del Lavoro, Istruzione, Ricerca e Università Servizio Ricerca e Innovazione Industriale for financial support through progetto POR FESR Abruzzo 2018-2020 Azione 1.1.1 e 1.1.4—“Studio di soluzioni innovative di prodotto e di processo basate sull’utilizzo industriale dei materiali avanzati” CUP n. C17H18000100007.

**Conflicts of Interest:** The authors declare no conflict of interest.

#### References

1. Yang, W.; Gan, L.; Li, H.; Zhai, T. Two-dimensional layered nanomaterials for gas-sensing applications. *Inorg. Chem. Front.* **2016**, *3*, 433–451. [[CrossRef](#)]
2. Donarelli, M.; Ottaviano, L. 2D Materials for Gas Sensing Applications: A Review on Graphene Oxide, MoS<sub>2</sub>, WS<sub>2</sub> and Phosphorene. *Sensors* **2018**, *18*, 3638. [[CrossRef](#)]
3. Late, D.J.; Huang, Y.K.; Liu, B.; Acharya, J.; Shirodkar, S.N.; Luo, J.; Yan, A.; Charles, D.; Waghmare, U.V.; Dravid, V.P.; et al. Sensing behavior of atomically thin-layered MoS<sub>2</sub> transistors. *ACS Nano* **2013**, *7*, 4879–4891. [[CrossRef](#)] [[PubMed](#)]
4. Liu, B.; Chen, L.; Liu, G.; Abbas, A.N.; Fathi, M.; Zhou, C. High-Performance Chemical Sensing Using Schottky-Contacted Chemical Vapor Deposition Grown Monolayer MoS<sub>2</sub> Transistors. *ACS Nano* **2014**, *8*, 5304–5314. [[CrossRef](#)] [[PubMed](#)]
5. Donarelli, M.; Prezioso, S.; Perrozzi, F.; Bisti, F.; Nardone, M.; Giancaterini, L.; Cantalini, C.; Ottaviano, L. Response to NO<sub>2</sub> and other gases of resistive chemically exfoliated MoS<sub>2</sub>-based gas sensors. *Sens. Actuators B Chem.* **2015**, *207*, 602–613. [[CrossRef](#)]
6. Kuru, C.; Choi, D.; Kargar, A.; Liu, C.H.; Yavuz, S.; Choi, C.; Jin, S.; Bandaru, P.R. High-performance flexible hydrogen sensor made of WS<sub>2</sub> nanosheet-Pd nanoparticle composite film. *Nanotechnology* **2016**, *27*, 195501. [[CrossRef](#)] [[PubMed](#)]
7. Perrozzi, F.; Emamjomeh, S.M.M.; Paolucci, V.; Taglieri, G.; Ottaviano, L.; Cantalini, C. Thermal stability of WS<sub>2</sub> flakes and gas sensing properties of WS<sub>2</sub>/WO<sub>3</sub> composite to H<sub>2</sub>, NH<sub>3</sub> and NO<sub>2</sub>. *Sens. Actuators B Chem.* **2017**, *243*, 812–822. [[CrossRef](#)]

8. Baek, J.; Yin, D.; Liu, N.; Omkaram, I.; Jung, C.; Im, H.; Hong, S.; Kim, S.M.; Hong, Y.K.; Hur, J.; et al. A highly sensitive chemical gas detecting transistor based on highly crystalline CVD-grown MoSe<sub>2</sub> films. *Nano Res.* **2017**, *10*, 1861–1871. [[CrossRef](#)]
9. Feng, Z.; Xie, Y.; Chen, J.; Yu, Y.; Zheng, S.; Zhang, R.; Li, Q.; Chen, X.; Sun, C.; Zhang, H.; et al. Highly sensitive MoTe<sub>2</sub> chemical sensor with fast recovery rate through gate biasing. *2D Mater.* **2017**, *4*, 025018. [[CrossRef](#)]
10. Cho, B.; Hahm, M.G.; Choi, M.; Yoon, J.; Kim, A.R.; Lee, Y.-J.; Park, S.-G.G.; Kwon, J.-D.D.; Kim, C.S.; Song, M.; et al. Charge-transfer-based gas sensing using atomic-layer MoS<sub>2</sub>. *Sci. Rep.* **2015**, *5*, 8052. [[CrossRef](#)]
11. Gao, J.; Li, B.; Tan, J.; Chow, P.; Lu, T.M.; Koratkar, N. Aging of Transition Metal Dichalcogenide Monolayers. *ACS Nano* **2016**, *10*, 2628–2635. [[CrossRef](#)] [[PubMed](#)]
12. Giancaterini, L.; Emamjomeh, S.M.; De Marcellis, A.; Palange, E.; Resmini, A.; Anselmi-Tamburini, U.; Cantalini, C. The influence of thermal and visible light activation modes on the NO<sub>2</sub> response of WO<sub>3</sub> nanofibers prepared by electrospinning. *Sens. Actuators B Chem.* **2016**, *229*, 387–395. [[CrossRef](#)]
13. Geng, X.; Lahem, D.; Zhang, C.; Li, C.-J.; Olivier, M.-G.; Debliquy, M. Visible light enhanced black NiO sensors for ppb-level NO<sub>2</sub> detection at room temperature. *Ceram. Int.* **2019**, *45*, 4253–4261. [[CrossRef](#)]
14. Hu, J.; Zou, C.; Su, Y.; Li, M.; Ye, X.; Cai, B.; Kong, E.S.-W.; Yang, Z.; Zhang, Y. Light-assisted recovery for a highly-sensitive NO<sub>2</sub> sensor based on RGO-CeO<sub>2</sub> hybrids. *Sens. Actuators B Chem.* **2018**, *270*, 119–129. [[CrossRef](#)]
15. Berholts, A.; Kahro, T.; Floren, A.; Alles, H.; Jaaniso, R. Photo-activated oxygen sensitivity of graphene at room temperature. *Appl. Phys. Lett.* **2014**, *105*, 163111. [[CrossRef](#)]
16. Huo, N.; Yang, S.; Wei, Z.; Li, S.-S.; Xia, J.-B.; Li, J. Photoresponsive and Gas Sensing Field-Effect Transistors based on Multilayer WS<sub>2</sub> Nanoflakes. *Sci. Rep.* **2015**, *4*, 5209. [[CrossRef](#)]
17. Ottaviano, L.; Palleschi, S.; Perrozzi, F.; D'Olimpio, G.; Priante, F.; Donarelli, M.; Benassi, P.; Nardone, M.; Gonchigsuren, M.; Gombosuren, M.; et al. Mechanical exfoliation and layer number identification of MoS<sub>2</sub> revisited. *2D Mater.* **2017**, *4*, 045013. [[CrossRef](#)]
18. Cho, B.; Yoon, J.; Lim, S.K.; Kim, A.R.; Kim, D.-H.; Park, S.-G.; Kwon, J.-D.; Lee, Y.-J.; Lee, K.-H.; Lee, B.H.; et al. Chemical Sensing of 2D Graphene/MoS<sub>2</sub> Heterostructure device. *ACS Appl. Mater. Interfaces* **2015**, *7*, 16775–16780. [[CrossRef](#)]
19. Long, H.; Harley-Trochimczyk, A.; Pham, T.; Tang, Z.; Shi, T.; Zettl, A.; Carraro, C.; Worsley, M.A.; Maboudian, R. High Surface Area MoS<sub>2</sub>/Graphene Hybrid Aerogel for Ultrasensitive NO<sub>2</sub> Detection. *Adv. Funct. Mater.* **2016**, *26*, 5158–5165. [[CrossRef](#)]
20. Niu, Y.; Jiao, W.C.; Wang, R.G.; Ding, G.M.; Huang, Y.F. Hybrid nanostructures combining graphene-MoS<sub>2</sub> quantum dots for gas sensing. *J. Mater. Chem. A* **2016**, *4*, 8198–8203. [[CrossRef](#)]
21. Yang, J.; Voiry, D.; Ahn, S.J.; Kang, D.; Kim, A.Y.; Chhowalla, M.; Shin, H.S. Two-dimensional hybrid nanosheets of tungsten disulfide and reduced graphene oxide as catalysts for enhanced hydrogen evolution. *Angew. Chem. Int. Ed.* **2013**, *52*, 13751–13754. [[CrossRef](#)] [[PubMed](#)]
22. Zhang, J.; Wang, Q.; Wang, L.; Li, X.; Huang, W. Layer-controllable WS<sub>2</sub>-reduced graphene oxide hybrid nanosheets with high electrocatalytic activity for hydrogen evolution. *Nanoscale* **2015**, *7*, 10391–10397. [[CrossRef](#)] [[PubMed](#)]
23. Jha, R.K.; Burman, D.; Santra, S.; Guha, P.K. WS<sub>2</sub>/GO Nanohybrids for Enhanced Relative Humidity Sensing at Room Temperature. *IEEE Sens. J.* **2017**, *17*, 7340–7347. [[CrossRef](#)]
24. Wang, X.; Gu, D.; Li, X.; Lin, S.; Zhao, S.; Romyantseva, M.N.; Gaskov, A.M. Reduced graphene oxide hybridized with WS<sub>2</sub> nanoflakes based heterojunctions for selective ammonia sensors at room temperature. *Sens. Actuators B Chem.* **2019**, *282*, 290–299. [[CrossRef](#)]
25. Treossi, E.; Melucci, M.; Liscio, A.; Gazzano, M.; Samori, P.; Palermo, V. High-Contrast Visualization of Graphene Oxide on Dye-Sensitized Glass, Quartz, and Silicon by Fluorescence Quenching. *J. Am. Chem. Soc.* **2009**, *131*, 15576–15577. [[CrossRef](#)] [[PubMed](#)]
26. Mao, X.; Xu, Y.; Xue, Q.; Wang, W.; Gao, D. Ferromagnetism in exfoliated tungsten disulfide nanosheets. *Nanoscale Res. Lett.* **2013**, *8*, 1–6. [[CrossRef](#)] [[PubMed](#)]
27. Stankovich, S.; Dikin, D.A.; Piner, R.D.; Kohlhaas, K.A.; Kleinhammes, A.; Jia, Y.; Wu, Y.; Nguyen, S.B.T.; Ruoff, R.S. Synthesis of graphene-based nanosheets via chemical reduction of exfoliated graphite oxide. *Carbon N. Y.* **2007**. [[CrossRef](#)]

28. Park, S.; Lee, K.S.; Bozoklu, G.; Cai, W.; Nguyen, S.B.T.; Ruoff, R.S. Graphene oxide papers modified by divalent ions—Enhancing mechanical properties via chemical cross-linking. *ACS Nano* **2008**. [[CrossRef](#)]
29. Prezioso, S.; Perrozzi, F.; Giancaterini, L.; Cantalini, C.; Treossi, E.; Palermo, V.; Nardone, M.; Santucci, S.; Ottaviano, L. Graphene Oxide as a Practical Solution to High Sensitivity Gas Sensing. *J. Phys. Chem. C* **2013**, *117*, 10683–10690. [[CrossRef](#)]
30. Di Paola, A.; Palmisano, L.; Venezia, A.M.; Augugliaro, V. Coupled Semiconductor Systems for Photocatalysis. Preparation and Characterization of Polycrystalline Mixed  $\text{WO}_3/\text{WS}_2$  Powders. *J. Phys. Chem. B* **1999**, *103*, 8236–8244. [[CrossRef](#)]
31. Wong, K.C.; Lu, X.; Cotter, J.; Eadie, D.T.; Wong, P.C.; Mitchell, K.A.R. Surface and friction characterization of  $\text{MoS}_2$  and  $\text{WS}_2$  third body thin films under simulated wheel/rail rolling-sliding contact. *Wear* **2008**, *264*, 526–534. [[CrossRef](#)]
32. Li, H.; Huang, M.; Cao, G. Markedly different adsorption behaviors of gas molecules on defective monolayer  $\text{MoS}_2$ : A first-principles study. *Phys. Chem. Chem. Phys.* **2016**, *18*, 15110–15117. [[CrossRef](#)] [[PubMed](#)]
33. Ma, D.; Wang, Q.; Li, T.; He, C.; Ma, B.; Tang, Y.; Lu, Z.; Yang, Z. Repairing sulfur vacancies in the  $\text{MoS}_2$  monolayer by using CO, NO and  $\text{NO}_2$  molecules. *J. Mater. Chem. C* **2016**, *4*, 7093–7101. [[CrossRef](#)]
34. Zhou, C.; Yang, W.; Zhu, H. Mechanism of charge transfer and its impacts on Fermi-level pinning for gas molecules adsorbed on monolayer  $\text{WS}_2$ . *J. Chem. Phys.* **2015**, *142*, 1–8. [[CrossRef](#)] [[PubMed](#)]
35. Bui, V.Q.; Pham, T.T.; Le, D.A.; Thi, C.M.; Le, H.M. A first-principles investigation of various gas ( $\text{CO}$ ,  $\text{H}_2\text{O}$ ,  $\text{NO}$ , and  $\text{O}_2$ ) absorptions on a  $\text{WS}_2$  monolayer: Stability and electronic properties. *J. Phys. Condens. Matter* **2015**, *27*, 305005. [[CrossRef](#)] [[PubMed](#)]
36. Bagsican, F.R.; Winchester, A.; Ghosh, S.; Zhang, X.; Ma, L.; Wang, M.; Murakami, H.; Talapatra, S.; Vajtai, R.; Ajayan, P.M.; et al. Adsorption energy of oxygen molecules on graphene and two-dimensional tungsten disulfide. *Sci. Rep.* **2017**, *7*, 1774. [[CrossRef](#)] [[PubMed](#)]
37. Guo, L.; Jiang, H.; Shao, R.; Zhang, Y.; Xie, S. Two-beam-laser interference mediated reduction, patterning and nanostructuring of graphene oxide for the production of a flexible humidity sensing device. *Carbon N. Y.* **2011**, *50*, 1667–1673. [[CrossRef](#)]



© 2019 by the authors. Licensee MDPI, Basel, Switzerland. This article is an open access article distributed under the terms and conditions of the Creative Commons Attribution (CC BY) license (<http://creativecommons.org/licenses/by/4.0/>).